Journal of Alloys and Compounds 489 (2010) 348–352

Contents lists available at ScienceDirect

Journal of Alloys and Compounds

journal homepage: www.elsevier.com/locate/jallcom

The influence of Sm doping in the electron-doped manganites $La_{0.9}Te_{0.1}MnO_3$

G.H. Zheng[a,b,*], Z.X. Dai[a,b], Y.Y. Zhang[a,b], Y.P. Sun[a,b]

[a] School of Physics and Material Science, Anhui University, Hefei 230039, PR China
[b] Key Laboratory of Materials Physics, Institute of Solid State Physics, Chinese Academy of Sciences, Hefei 230031, PR China

ARTICLE INFO

Article history:
Received 23 February 2009
Received in revised form
16 September 2009
Accepted 22 September 2009
Available online 30 September 2009

PACS:
67.55.Hc
74.25.Fy

Keywords:
Structural properties
Transport mechanism

ABSTRACT

The effect of Sm-doping on structural, magnetic and transport properties in the electron-doped manganites $La_{0.9-x}Sm_xTe_{0.1}MnO_3$ ($0 \le x \le 0.15$) with fixed carrier concentration is investigated. All samples show rhombohedral structure with the space group $R\bar{3}C$. Both the Curie temperature T_C and magnetization M of samples decrease with increasing Sm-doping level. For all samples, there exists two metal–insulator (M–I) transitions in the temperature dependence of the resistivity curves $\rho(T)$. The resistivity of the sample increases with increasing Sm-doping level. By fitting the$\rho(T)$ data in the high paramagnetic (PM) region, it is found that the transport properties are dominated by the small polaron conduction (SPC) mechanism. With increasing Sm-doping level, the polaron binding energy increases, which is ascribed to the lattice distortion due to the Sm doping.

1. Introduction

The $A_{1-x}D_xMnO_3$ perovskites manganites are interesting systems because of the anomalous magnetic and transport properties exhibited by them such as colossal magnetoresistance (CMR), metal–insulator (M–I) transition, antiferromagnetic–ferromagnetic (AFM–FM) ordering, and lattice dynamics associated with phase transitions [1–3]. Zener's double exchange (DE) interaction between Mn ions through charge carriers in the oxygen 2p orbitals was introduced in order to explain the coupling of magnetic and electronic properties in these compounds [4]. However, many studies have shown that DE interaction is not sufficient to explain the complex physics in these compounds, especially with regard to the lattice distortions coinciding with the emergence of CMR [5–7]. In addition, the phase separation [8] (PS) has also been suggested to play an important role.

In order to understand the unusual magnetic and transport properties of doped perovskites $A_{1-x}D_xMnO_3$, many studies have been carried out by doping the trivalent rare earth sites (A site) with divalent atoms (Ca, Sr, Ba, etc.) [9–11] or tetravalent atoms (Te, Zr, Ce) [12–14]. It has shown that the average ionic size of cations (R, A) [15,16], the size mismatch between R and A cations [17] contributes to the physical properties of this system. The study of Hwang et al. [15] on $(La_{1-x}R_x)_{0.7}Ca_{0.3}MnO_3$ reveals that the T_C and the conductivity decrease when some La^{3+} is replaced by Pr^{3+} or Y^{3+}, in other words, the magnetic and transport properties of the system are a strong function of average A size ionic radius, $\langle r_A \rangle$. They have concluded that the electronic and magnetic state are highly relevant to a geometrical index called the Goldsmith tolerance factor t, which decides the crystallographic distortions from the cubic ($t = 1$) perovskite structure. The Goldsmith tolerance factor, describing the stability of the perovskite structure, is defined as $t = (r_A + r_O)/\sqrt{2}(r_B + r_O)$. In such a definition, r_i (i = A, B, or O) represents the average ionic size of each element. With decreasing t, the Mn–O–Mn bond angle, to which the transfer integral is related and which describes the electron hopping between Mn^{3+} and Mn^{4+}, decreases. Therefore, in order to better understand the physical properties of the electron-doped manganites $La_{0.9}Te_{0.1}MnO_3$ with the change of the A-site ionic radii, we studied the effects of the partial substitution of Sm for La with fixed Mn^{2+}/Mn^{3+} ratio at 1/9. The structure, resistivity ρ, magnetization M measurement results of $La_{0.9-x}Sm_xTe_{0.1}MnO_3$ ($0 \le x \le 0.15$) compound have been presented and discussed in this text.

2. Experimental

Polycrystalline samples with nominal compositions $La_{0.9-x}Sm_xTe_{0.1}MnO_3$ ($0 \le x \le 0.15$) were prepared by solid-state reaction method. Stoichiometric high-purity La_2O_3, Sm_2O_3, TeO_2 and MnO_2 powders were mixed and ground, and then heated in air at 750 °C for 24 h. The powder obtained was ground, pelletized, and sintered at 1100 °C for 24 h with three intermediate grinding, and finally, the furnace was cooled down to the room temperature. The structure and lattice constant were determined by powder X-ray diffraction using Cu Kα radiation at

---

[*] Corresponding author at: School of Physics and Material Science, Anhui University, Hefei 230039, PR China.
E-mail address: ghzheng@issp.ac.cn (G.H. Zheng).

0925-8388/$ – see front matter © 2009 Elsevier B.V. All rights reserved.
doi:10.1016/j.jallcom.2009.09.130

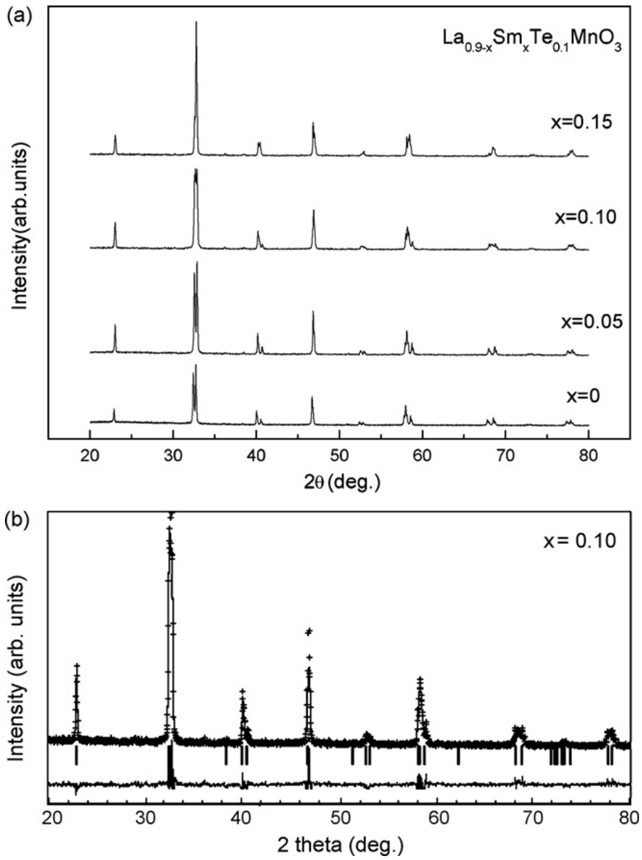

Fig. 1. (a) XRD patterns of $La_{0.9-x}Sm_xTe_{0.1}MnO_3$ ($0 \le x \le 0.15$) compounds at the room temperature. (b) The experimental and calculated XRD patterns of the sample with $x = 0.10$. Crosses indicate the experimental data and the calculated data is continuous line overlapping them. The lowest curve shows the difference between experimental and calculated patterns. The vertical bars indicated the expected reflection positions.

the room temperature. The magnetic measurements were performed on a Quantum Design superconducting quantum interference device (SQUID) MPMS system ($1.8\,K \le T \le 400\,K$, $0\,T \le H \le 5\,T$). The temperature dependence of ρ was measured by the standard four-probe from 5 to 350 K at zero field in a commercial Quantum Design Physical Property Measurements System (PPMS) ($1.8\,K \le T \le 400\,K$, $0\,T \le H \le 9\,T$).

3. Results and discussion

3.1. Structural properties

Fig. 1a shows that X-ray diffraction patterns of $La_{0.9-x}Sm_xTe_{0.1}MnO_3$ ($0 \le x \le 0.15$) at room temperature. All the samples are single phase with no detectable secondary phases. XRD patterns for all samples can be indexed by rhombohedral lattice with the space group $R\bar{3}C$. The experimental and calculated XRD patterns for the sample with $x = 0.10$ are presented in Fig. 1b. The structural parameters are refined by the standard Rietveld technique [18] and the fitting between the experimental spectra and the calculated values is relatively good based on the consideration of lower RP values as shown in Table 1.

Fig. 2a plots the Mn–O–Mn bond angle and Mn–O length extracted from the Rietveld refinement at room temperature. The Mn–O–Mn bond angle decreases with increasing the doping level x, whereas the Mn–O bond length increases which displays the inverse correlation to the variation in the Mn–O–Mn bond angle. It is well known that there are two possible origins of the lattice distortion of the perovskite structures: one is the deformation of the $Mn^{3+}O_6$ octahedra, originating from the Jahn–Teller (J–T) effect which is decided by the concentration of Mn^{3+} ions, and the other is the variation of the average ionic radius of the A-site element $\langle r_A \rangle$. In the present samples, the concentration of Mn^{3+} is fixed and the lattice distortion is ascribed to the variation of the average A-site radius $\langle r_A \rangle$, induced by the substitution of smaller Sm^{3+} ($r = 0.113$ nm) for larger La^{3+}($r = 0.122$ nm) ions. The exchange interaction between the Mn–Mn depends on the bond angle and the bond length. The increase of Mn–O length and decrease of Mn–O–Mn bond angle weaken the Mn–Mn exchange interaction, leading to a lower magnetic ordering temperature and a smaller magnetization magnitude value (see later discussion of M–T curves). At the same time, the reduction in Mn–O–Mn bond angle provides a local trap of e_g electrons, and then leads to the increase of resistivity and the activation energy of electron hopping (as discussed below).

Table 1
Refined structural parameters of $La_{0.9-x}Sm_xTe_{0.1}MnO_3$ ($0 \le x \le 0.15$) at room temperature.

Parameter	$x = 0$	$x = 0.05$	$x = 0.10$	$x = 0.15$
a (nm)	0.54761	0.54851	0.54862	0.54878
c (nm)	1.3228	1.3264	1.3265	1.3266
v (nm^3)	0.33025	0.33237	0.33660	0.33853
$d_{(Mn-O)}$ (nm)	0.18401	0.18426	0.18505	0.18623
$\langle$Mn–O–Mn$\rangle$ (°)	167.09	166.63	163.65	160.92
W	0.1176	0.1146	0.1113	0.1072
R_p (%)	9.04	8.38	8.01	8.99

The electronic bandwidth W has been used to discuss magnetic and transport properties of perovskites with varied A-site

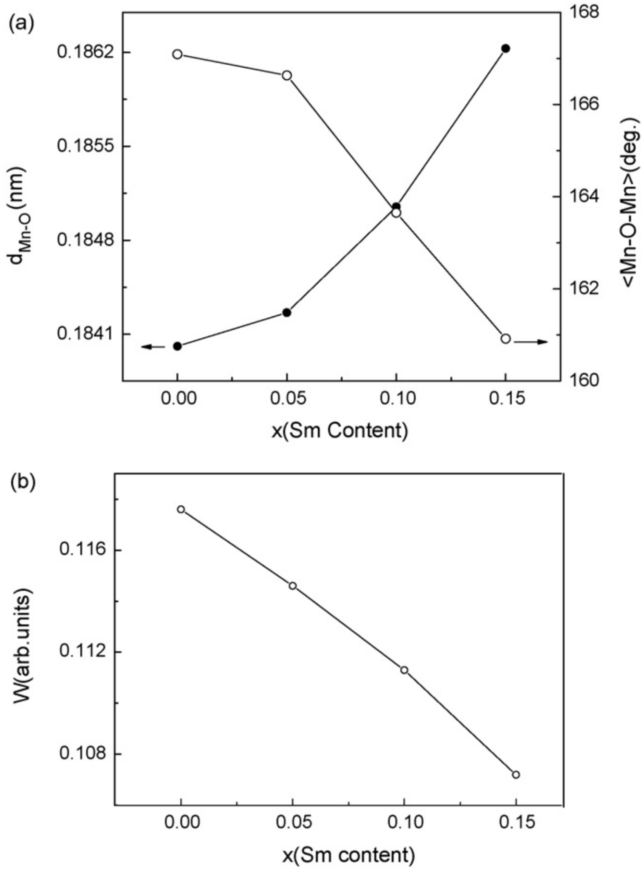

Fig. 2. (a) The Mn–O bond length and Mn–O bond angle for $La_{0.9-x}Sm_xTe_{0.1}MnO_3$ ($0 \le x \le 0.15$) as a function of the Sm concentration, determined from the room temperature XRD. (b) The electronic bandwidth for $La_{0.9-x}Sm_xTe_{0.1}MnO_3$ ($0 \le x \le 0.15$) as a function of the Sm concentration, determined from the room temperature XRD.

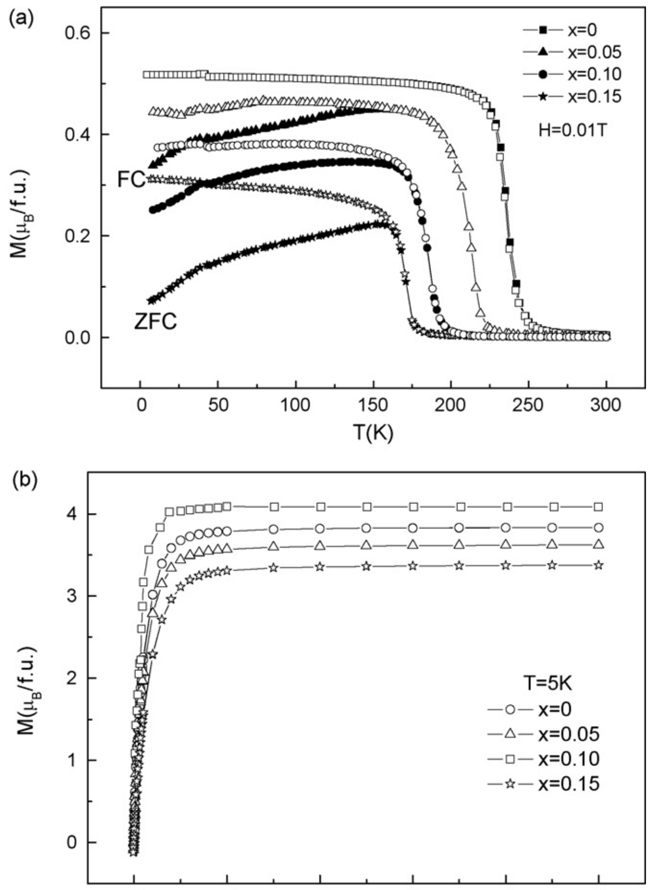

Fig. 3. (a) Temperature dependence of the magnetization for $La_{0.9-x}Sm_xTe_{0.1}MnO_3$ ($0 \le x \le 0.15$) measured in both zero-field cooling (ZFC) and field cooling (FC) modes at an applied magnetic field of $H = 0.01$ T. (b) Field dependence of the magnetization in $La_{0.9-x}Sm_xTe_{0.1}MnO_3$ ($0 \le x \le 0.15$) at 5 K.

Table 2
Electrical and magnetic parameters of $La_{0.9-x}Sm_xTe_{0.1}MnO_3$ ($x = 0$, 0.05, 0.10 and 0.15).

Parameter	$x = 0$	$x = 0.05$	$x = 0.10$	$x = 0.15$
T_C (K)	238	212	188	170
T_{P1} (K)	240	218	190	–
T_{P2} (K)	192	172	137	–
T_S (K)	240	216	204	177
T_κ (K)	245	215	185	–
E_S (meV)	11	17	22	23
E_ρ (meV)	115	123	132	134
E_b (meV)	208	210	220	222

Both E_ρ and E_S are the activation energies by fitting $\rho(T)$ and $S(T)$ curves according to SPC model for all samples in the PM region. E_b is the binding energy for the polaron.

doping [15,19]. The empirical formula of the bandwidth W for ABO_3-type perovskites using the tight binding approximation [20] is $W \propto \cos\omega/(d_{Mn-O})^{3.5}$, where $\omega = 0.5(\pi - \langle Mn–O–Mn \rangle)$ and d_{Mn-O} is the Mn–O bond length. The calculated values of $\cos\omega/(d_{Mn-O})^{3.5}$ using the refinement results are shown in Fig. 2b. We assume the bandwidth W is proportional to the values of $\cos\omega/(d_{Mn-O})^{3.5}$. It is found that the bandwidth W decreases with increasing the Sm content. The evolution of bandwidth W follows the change in the ⟨Mn–O–Mn⟩ bond angle. The decrease in bandwidth reduces the overlap between the O–2p and the Mn–3d orbitals, which in turn decreases the exchange coupling of Mn^{2+}–Mn^{3+}.

3.2. Magnetic properties

Fig. 3a shows the temperature dependence of magnetization M of $La_{0.9-x}Sm_xTe_{0.1}MnO_3$ ($0 \le x \le 0.15$) under both zero-field cooling (ZFC) and field cooling (FC) modes at $H = 0.1$ T. All samples exhibit FM–paramagnetic (FM–PM) transition. The Curie temperatures T_C (defined as the one corresponding to the point of change-in-slope in the M vs. T curve) is 238, 212, 188, and 170 K for $x = 0$, 0.05, 0.10, and 0.15, respectively. The data are listed in Table 2. Obviously, Sm doping drives T_C to lower temperatures. In addition, the magnitude of magnetization M also decreases with increasing Sm-doping level. The phenomena can be interpreted as the reduction of Mn–O–Mn bond angle with decreasing the average A-site element $\langle r_A \rangle$ due to the partial substitution of smaller Sm^{3+} ions for larger La^{3+} ions as discussion above. This substitution causes the narrowing of the bandwidth and the decreasing of mobility of e_g electrons, and results in the weakness of DE interaction. In addition, from Fig. 3a it can be seen that the ZFC curves does not coincide with the FC curves at low temperatures for $x \ge 0.05$ samples. The discrepancy between ZFC and FC $M(T)$ curves can be due to the total effect from magnetic inhomogeneity and domain wall [21].

The magnetization M as a function of the applied magnetic field H at $T = 5$ K is shown in Fig. 3b for all samples. It shows that the magnetization reaches saturation at about 1 T and keeps constant up to 5 T for all samples, which is considered as the result of the rotation of the magnetic domain under the action of an applied magnetic field. The saturation magnetization μ_S is 4.08 μ_B, 3.83 μ_B, 3.62 μ_B and 3.37 μ_B for $x = 0$, 0.05, 0.10 and 0.15, respectively. It can be seen that the value of μ_S become smaller with increasing the doping level x. We suggest that it is related to the spin disorder and the localization of e_g electrons. That is to say, the DE interaction becomes weak when the Sm-doped level increases, and correspondingly results in the decrease of the averaged ordered moment of sum of the t_{2g} spins and the forcibly aligned e_g spins on the identical Mn site.

3.3. Electrical properties

Fig. 4 shows the resistivity as a function of temperature $\rho(T)$ for all samples at zero field in the temperature range of 5–350 K. For the sample with $x = 0$, it shows that there exists a M–I transition at T_{P1} (=240 K), which is close to its Curie temperature T_C (=238 K). In addition, there exists a shoulder at T_{P2} (=192 K) below T_{P1}, which is similar to the double peak behavior observed usually in alkaline-earth-metal-doped and alkali-metal-doped samples of $LaMnO_3$ [13,22,23]. With increasing the Sm-doping level, both T_{P1} and T_{P2} move to lower temperatures. T_{P1} is 218 K and T_{P2} is 172 K for the sample with $x = 0.05$. T_{P1} is 190 K and T_{P2} is 137 K for the sample with $x = 0.10$. When the Sm content reaches $x = 0.15$, T_{P1} moves to 190 K and T_{P2} shifts to 137 K. The T_{P1} and T_{P2} data are also presented in Table 2. Moreover, it is obvious that the resistivity increases with increasing Sm-doping level. The phenomenon is usually explained according to the decreased average ionic radius of the A-site element $\langle r_A \rangle$ with increasing doping level x, which reduces the FM coupling due to reduced band width of e_g electron.

The resistivity data for all samples under the applied magnetic field $H = 5$ T is also recorded in Fig. 4. It is observed that T_{P1} and T_{P2} moves toward lower temperature, and the resistivity of the samples decreases under the applied magnetic field. And it leads to negative MR. Temperature dependence of the MR of samples is presented in Fig. 5. Here the MR is defined as $MR = (\rho_0 - \rho_H)/\rho_0 \times 100$ (%), where ρ_0 is the resistivity at zero field and ρ_H is the resistivity at $H = 5$ T. For all samples, there are two peaks corresponding to T_{P1} and T_{P2}. Moreover, with increasing Sm-doping level, the peak at T_{P1} becomes weak and the bump at T_{P2} becomes obvious as observed in MR(T) curves, which is in accordance with the $\rho(T)$ behavior.

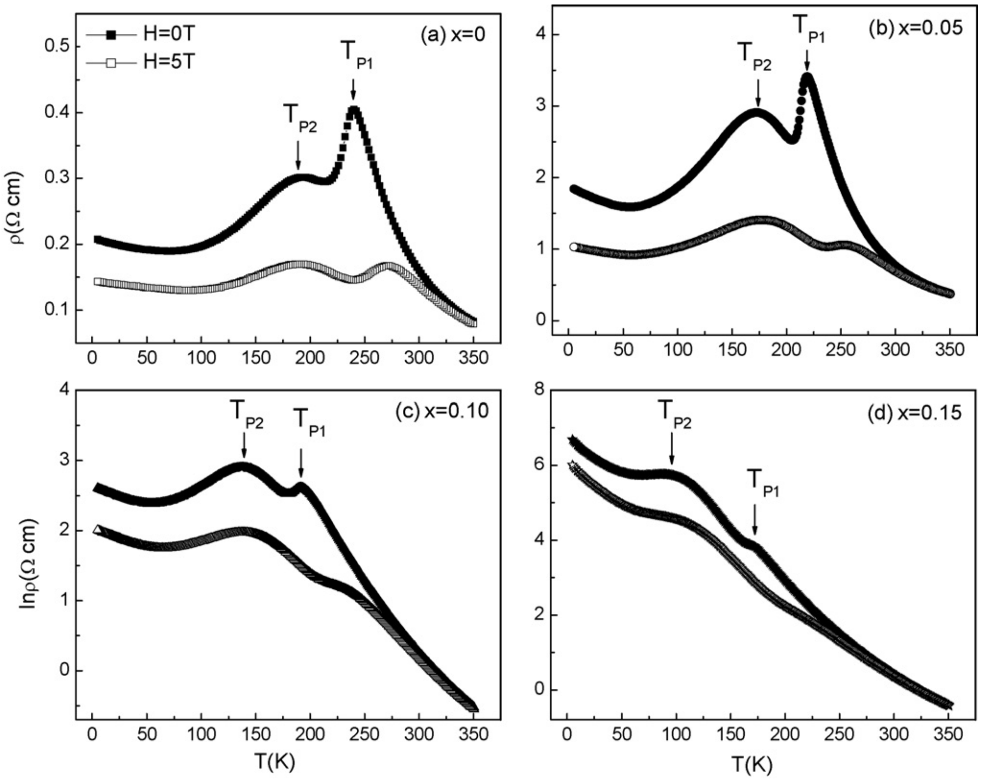

Fig. 4. Temperature dependence of the resistivity $\rho(T)$ of the compound $La_{0.9-x}Sm_xTe_{0.1}MnO_3$ ($0 \le x \le 0.15$) at $H = 0$ and 5 T.

According to the DE model, in the homogeneous FM state, the electrons are mobile and the FM state and metallic state should accompany and facilitate each other. In contrast, the transport property of the studied samples does not fully show metallic state below T_C. The FM order at low temperatures for the studied samples can be understood by the presence of FM clusters. On the one hand, based on the coexistence of FM clusters and AFM insulating phase in the low temperature region, we may suggest that the spatially inhomogeneous metallic and insulating areas coexist in the studied samples [24]. When the system is transferred from PM to FM phase with decreasing temperatures, the transport property of the samples does not fully show the metallic state because the FM metallic (FMM) phases are disconnected for the existence of the FM insulating (FMI) phases among them. With further decrease of temperature below T_C or under the applied magnetic field, the FMI region decreases and the metallic phases are connected in a percolative manner.

Next, we discuss the electronic transport mechanism for our studied samples. The $\rho(T)$ data in the high temperature PM region are fitted by purely thermally activated conduction (TAC) law, $\rho(T) = \rho 0 \exp(E_0/k_BT)$, the adiabatic small polaronic conduction (SPC), $\rho(T) = BT\exp(E_0/k_BT)$, and Mott's variable-range-hopping (VRH), $\rho(T) = \rho_0 \exp[(T_0/T)^{1/4}]$. The $\rho(T)$ curves of all samples are plotted as $\ln(\rho/T)$ vs. $1000/T$ as shown in Fig. 6. The solid lines correspond to the experimental data and the dashed lines denote the fitted results in terms of the SPC model. From this fits, the activation energy E_ρ can be obtained. The data are also summarized in Table 2. It can be seen that E_ρ rises with increasing the doping level x. The

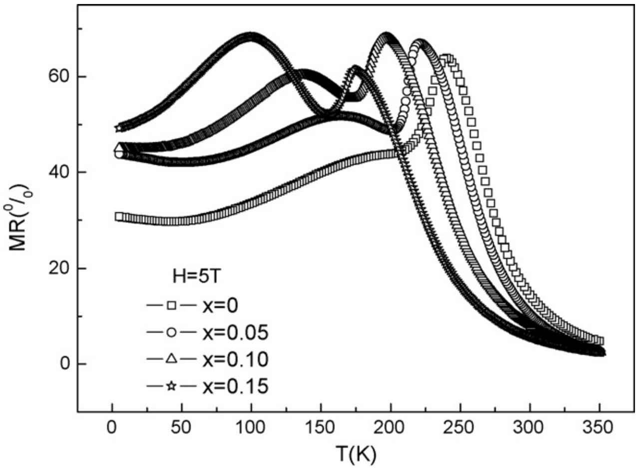

Fig. 5. Temperature dependence of magnetoresistance (MR) for the compound $La_{0.9-x}Sm_xTe_{0.1}MnO_3$ ($0 \le x \le 0.15$).

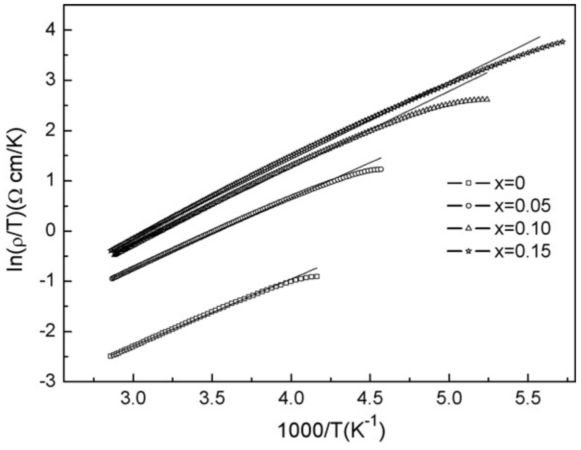

Fig. 6. The fitting plot of $\rho(T)$ curves of $La_{0.9-x}Sm_xTe_{0.1}MnO_3$ ($0 \le x \le 0.15$) according to SPC model. The solid lines represent the experimental data and the dashed lines correspond to the fitting curves.

polaron activation energy is normally assumed to be the sum of the relevant parts: $E_\rho = E_S + W_H$. Here W_H is the polaronic hopping energy, and is equal to one-half of the polaron binding energy E_b. E_S is the energy required to activate the hopping of carriers.

4. Conclusion

The structure, magnetization and resistivity have been studied for the electron-doped manganites $La_{0.9-x}Sm_xTe_{0.1}MnO_3$ ($0 \le x \le 0.15$). All samples show a rhombohedral structure with the space group $R\bar{3}C$. The substitution of smaller size Sm at the La site shifts both the M–I transition temperature and the Curie temperature T_C to lower values. With increasing Sm-doping level, the resistivity increases and the magnetization decreases. For all samples, there exist two M-I transitions. By fitting $\rho(T)$ curves, it is found that the SPC mechanism dominates the electron conduction of the high PM region. The increase of the polaron binding energy is ascribed to the increase of lattice distortion due to the Sm doping.

Acknowledgements

This work was supported by the National Key Research under contract No. 001CB610604, the National Nature Science Foundation of China under contract No.10474100, 10374033, the Fundamental Bureau of the Chinese Academy of Sciences, and Anhui College provincial level natural sciences research project No. KJ2007B130.

References

[1] R. von Helmolt, J. Wecker, B. Holzapfel, L. Schultz, K. Samwer, Phys. Rev. Lett. 71 (1993) 2331.
[2] A. Urushibara, Y. Moritomo, T. Arima, A. Asamitsu, G. Kido, Y. Tokura, Phys. Rev. B 51 (1995) 14103.
[3] Y. Tomioka, A. Asamitsu, H. Kuwahara, Y. Moritomo, Y. Tokura, Phys. Rev. B 53 (1996) R1689.
[4] C. Zener, Phys. Rev. 82 (1951) 403.
[5] A.J. Millis, P.B. Littlewood, B.I. Shraiman, Phys. Rev. Lett. 74 (1995) 5144.
[6] A.J. Millis, B.I. Shraiman, R. Mueller, Phys. Rev. Lett. 77 (1996) 175.
[7] A.J. Millis, Phys. Rev. B 53 (1996) 8434.
[8] M. Uehara, S. Mori, C.H. Chen, S.-W. Cheong, Nature 399 (1999) 560;
A. Moreo, S. Yunoki, E. Dagotto, Science 283 (1999) 2034;
M. Fath, S. Freisem, A.A. Menovsky, Y. Tomiooka, J. Aarts, J.A. Mydosh, Science 285 (1995) 1540.
[9] J.J. Neumeier, K. Andres, K.J. McClellan, Phys. Rev. B 59 (1999) 1701.
[10] M. Medarde, J. Mesot, P. Lacorre, S. Rosenkranz, P. Fischer, K. Gobrecht, Phys. Rev. B 52 (1999) 9248.
[11] M. Muroi, R. Street, P.G. McCormick, J. Appl. Phys. 87 (2000) 3424.
[12] P. Mandal, S. Das, Phys. Rev. B 56 (1997) 15073.
[13] S. Roy, N. Ali, J. Appl. Phys. 89 (2001) 7425.
[14] G.T. Tan, S.Y. Dai, P. Duan, Y.L. Zhou, H.B. Lu, Z.H. Chen, J. Appl. Phys. 93 (2003) 5480.
[15] H.Y. Hwang, S.-W. Cheong, P.G. Radaelli, M. Marezio, B. Batlogg, Phys. Rev. Lett. 75 (1995) 914.
[16] J. Blasco, J. García, J.M. de Tereas, M.R. Ibarra, P.A. Algarabel, C. Marquina, J. Phys.: Condens. Matter. 8 (1996) 7427.
[17] L.M. Rodriguez-Martinez, J.P. Attfield, Phys. Rev. B 54 (1996) R15622.
[18] D.B. Wiles, R.A. Young, J. Appl. Crystallogr. 14 (1981) 149.
[19] H. Kobayashi, H. Akutsu, E. Arai, H. Tanaka, A. Kobayashi, Phys. Rev. B 56 (1997) 8526.
[20] M. Medarde, J. Mesot, P. Lacorre, S. Rosenkranz, P. Fischer, K. Gobrecht, Phys. Rev. B 52 (1995) 9248.
[21] C. Raj Sankar, P.A. Joy, Phys. Rev. B 72 (2004) 24405;
X.L. Wang, S.J. Kennedy, H.K. Liu, S.X. Dou, J. Appl. Phys. 83 (1998) 7177.
[22] S.L. Ye, W.H. Song, J.M. Dai, S.G. Wang, K.Y. Wang, G.L. Yuan, Y.P. Sun, J. Appl. Phys. 88 (2000) 5915.
[23] N. Zhang, W.P. Ding, W. Zhong, D.Y. Xing, Y.W. Du, Phys. Rev. B 56 (1997) 8138.
[24] B. Vertruyen, R. Cloots, A. Rulmont, G. Dhalenne, M. Ausloos, Ph. Vanderbemden, J. Appl. Phys. 90 (2001) 5692;
B.I. Belevtsev, D.G. Naugle, K.D.D. Rathnayaka, A. Parasiris, J. Fink-Finowicki, Physica B 355 (2005) 341;
J.M.D. Coey, M. Viret, S. Von Molnar, Adv. Phys. 48 (1999) 167.